JACS
JOURNAL OF THE AMERICAN CHEMICAL SOCIETY
pubs.acs.org/JACS
Article

Bifunctional D−π−A Ligand Directs Self-Organized Interface Passivation for Efficient Perovskite Photovoltaics

Bowei Li, Yahong Pu, Chi Chen, Jing Chen, Zhixiao Qin, Qing Lian,* Wenji Zhan, Chujun Zhang, Zhenhuang Su, Jiahao Guo, Bin Liu, Jiasheng Su, Anran Yu, Yu Zou, Yao Wang, Yuetian Chen, Yanfeng Miao, Junliang Yang, Yiqiang Zhan, Zhao-Kui Wang, Anlian Pan, Yan-Fang Zhang,* Yanming Wang,* Xugang Guo,* Shixuan Du, and Yixin Zhao*

Cite This: J. Am. Chem. Soc. 2026, 148, 13433−13443
Read Online
ACCESS | Metrics & More | Article Recommendations | Supporting Information

ABSTRACT: Passivating engineering has emerged as one of the most important strategies for improving the performance and stability of perovskite solar cells (PSCs). However, most post-treatment or buried-in passivation approaches are depth-dependent, where separate agents target either bulk or interfacial defects, complicating film processing and limiting large-scale fabrication. Here, we report a bifunctional D−π−A passivating ligand, triphenylamine-furan-cyanoacrylic acid (TPA-FCA), which integrates a hydrophilic anchoring group with a bulky hydrophobic donor−π scaffold. Such bifunctional TPA-FCA self-organizes within the as-crystallized perovskite film, vertically segregating to both interfaces and simultaneously passivating the defects in the perovskite bulk and at adjacent interfaces. This characteristic enables TPA-FCA to suppress both nonradiative and charge-transport losses in the complete PSCs. Consequently, PSCs incorporating TPA-FCA deliver a champion efficiency of 26.56% (26.37% certified) together with remarkable operational stability. Under continuous maximum power point tracking at 65 °C (ISOS-L-2), the unencapsulated TPA-FCA device maintains 90% of its initial efficiency after 1400 h (T_{90} = 1400 h). Further fabrication of large-area (30 cm × 30 cm) perovskite submodules demonstrates the passivation efficacy of the TPA-FCA, yielding a certified efficiency of 21.93%. This work provides fundamental insights into self-organized ligands and demonstrates an applicable molecular design strategy for high-performance, stable, and scalable perovskite photovoltaics.

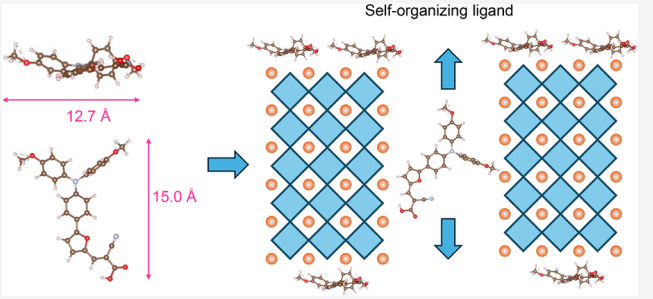

INTRODUCTION

Metal halide perovskites have emerged as promising semiconductor materials for many optoelectronic applications, including solar cells, light-emitting diodes, and photodetectors.[1] Their rapid development is driven by a combination of favorable attributes, such as tunable crystal size and bandgap, long electron−hole lifetime, and carrier diffusion length.[2] In terms of processing, perovskites are compatible with low-temperature, high-throughput deposition techniques that can be integrated into flexible or rigid, small- or large-area substrates. As a result, perovskite solar cells (PSCs), in both single-junction and tandem configurations, have achieved remarkable power conversion efficiencies (PCEs) compared to conventional III−V semiconductor and organic photovoltaics.[3]

To advance the performance of PSCs, optimizing the quality of the perovskite absorber layer is crucial. A wide range of molecular additives, ranging from small molecules to polymers,[4−6] have been introduced into the formulation of the perovskite precursor solution or ink. Effective additives can promote crystallization and enhance the optoelectronic properties of the prepared perovskite films. Among these, certain additives function as ligands, typically organic molecules, that can interact with undercoordinated metal sites (e.g., Pb^{2+}) or halide vacancies.[5] These ligand-perovskite interactions, often occurring at surfaces or grain boundaries, play a pivotal role in passivating trap states and suppressing nonradiative recombination. However, given the spatial distribution of defects in the perovskite layer,[7] effective passivating ligands must consider both the bulk and the adjacent interfaces.

Due to the out-of-plane growth of perovskite films, the vertical distribution of ligands becomes a critical factor that remains insufficiently understood. Ligand diffusion is a

Received: February 4, 2026
Revised: March 6, 2026
Accepted: March 10, 2026
Published: March 17, 2026

https://doi.org/10.1021/jacs.6c02548
J. Am. Chem. Soc. 2026, 148, 13433−13443

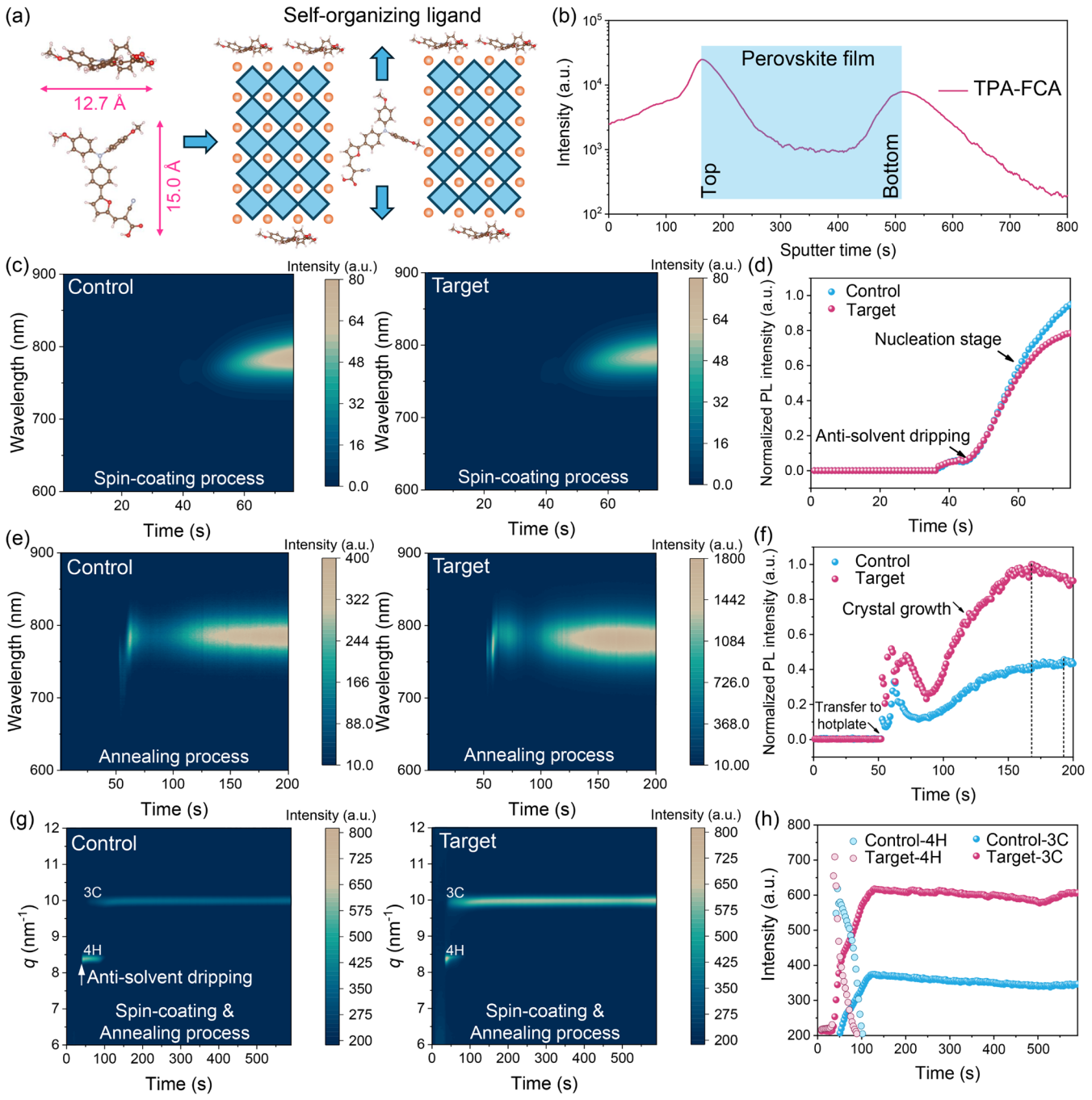

Figure 1. TPA-FCA and its self-organizing effect in a perovskite film. (a) Chemical structure of TPA-FCA, acting as the additive ligand in the preparation of a perovskite solution and a schematic of the as-crystallized perovskite film, highlighting the self-organizing effect of TPA-FCA. (b) ToF-SIMS depth profile of TPA-FCA obtained from a stack of glass/FTO/perovskite/C_{60}. In situ PL measurements acquired during the (c) spin-coating and (e) annealing processes of control and TPA-FCA-treated perovskite films. (d,f) Corresponding evolution of the maximum PL intensity. PL acquisition started prior to the spin-coating program and hot plate annealing; dashed lines indicate the maximum PL intensity. (g) In situ GIWAXS measurements of the control and TPA-FCA-treated films. (h) Corresponding intensity evolution of the diffraction peaks at q = 8.4 nm^{-1} and 10.0 nm^{-1}. The GIWAXS patterns were collected at an angle of incidence of 1°.

common phenomenon. In our previous studies, we even observed it when ligands were introduced by post-treatment onto the charge transport layer beneath the perovskite.[8] Controlling the ligand diffusion is hard to achieve, as it could be redistributed during the perovskite crystallization, e.g., either aggregating on top or near the bottom surface of the final film.[6,9] This nonuniform distribution often limits the passivation efficiency and reproducibility of device fabrication, particularly for large-area PSCs, where achieving uniform passivation across tens of square centimeters is difficult. To overcome these limitations, we propose a molecular design strategy that enables depth-targeted passivation. A single molecule with spontaneous distribution in perovskite films may offer a more controlled and efficient route toward spatially comprehensive passivation in PSCs. Additionally, this behavior can minimize the need for supplementary passivation agents or

https://doi.org/10.1021/jacs.6c02548
J. Am. Chem. Soc. 2026, 148, 13433−13443

interfacial modifiers, simplifying the fabrication process and improving reproducibility across small- and large-area devices.

In this work, we introduced a donor−π−acceptor (D−π−A) passivating ligand, triphenylamine-furan-cyanoacrylic acid (TPA-FCA). Based on the depth profile, TPA-FCA exhibits a dumbbell-shaped aggregation in the as-crystallized perovskite film, leading to self-organization near both the top surface and buried interface. Further crystal growth modeling demonstrates that TPA-FCA directs nucleation at the dual sides of the perovskite, promoting bidirectional crystal growth toward the film center. As a result, TPA-FCA can effectively enhance the perovskite quality and simultaneously passivate the interfaces between the hole or electron transporters and perovskite layers. By suppressing nonradiative and charge-transport recombination losses, the TPA-FCA ligand improves the performance of the fabricated PSCs, achieving a champion efficiency of 26.56% (26.37% certified). Furthermore, the same strategy enables the fabrication of 30 × 30 cm perovskite submodules with a certified efficiency of 21.93%. More encouragingly, the unencapsulated device exhibits excellent operational stability, retaining 90% of its initial efficiency over 1400 h under continuous maximum power point tracking at 65 °C, consistent with the ISOS-L-2 protocol. These results provide a blueprint for molecular design strategies that simultaneously address bulk and interfacial defects in PSCs.

RESULTS AND DISCUSSION

Self-Organizing Mechanism of TPA-FCA

We synthesized a D−π−A molecule, triphenylamine-furan-cyanoacrylic acid (TPA-FCA; the synthesis route is shown in Figure S1), with triphenylamine as the donor, furan as the π-conjugated bridge, and cyanoacrylic acid as the acceptor. The chemical structure of TPA-FCA is confirmed by proton nuclear magnetic resonance (^{1}H NMR, Figure S2) and mass spectrometry measurements (Figure S3). TPA-FCA was then added to the perovskite solution, but it cannot significantly change the colloid size suggested by dynamic light scattering (DLS) measurements (Figure S4). This indicates that TPA-FCA ensures a uniform precursor distribution, which is critical for forming high-quality films. During film deposition, TPA-FCA will participate in the whole crystallization of the perovskite, involving nucleation (e.g., homogeneous and heterogeneous) and crystal growth process.[10] Due to the large molecular size, TPA-FCA cannot go into the perovskite lattice, as the ionic radius >2.5 Å leads to an unstable structure suggested by the Goldsmith factor.[11] The similar X-ray diffraction (XRD) patterns indicate that TPA-FCA does not alter the bulk crystal structure of the perovskite and is, therefore, likely located at the grain boundaries (Figure S5). Consistently, the control and TPA-FCA-treated films show comparable grain sizes, excluding morphology-related effects (Figure S6).

Featuring an amphiphilic nature with an anchoring group and a bulky moiety, TPA-FCA could affect the perovskite crystallization and the ligand distribution.[11] Specifically, the hydrophilic cyanoacrylic acid group can enhance perovskite deposition and minimize the defects at both the bottom (substrate) and top (air-exposed) surfaces through strong coordination with Pb^{2+} ions.[12,13] The hydrophobic triphenylamine can provide a π-conjugated scaffold that drives molecular stacking and enriches the ligand at the film interfaces,[14] thereby guiding interfacial nucleation while suppressing uncontrolled bulk nucleation. Following this reasoning, TPA-FCA is expected to redistribute within the final perovskite film, leading to differential accumulation in the bulk and at the surface (Figure 1a). To probe the vertical distribution of TPA-FCA, we conducted the time-of-flight secondary-ion mass spectroscopy (ToF-SIMS). In the cross-sectional perovskite film, the depth profiling of ion species reveals that TPA-FCA is predominantly enriched at both the top and bottom interfaces (Figure 1b, Figure S7). This spatial distribution indicates that TPA-FCA is excluded from lattice incorporation during crystallization and instead segregates to the interfaces, leading to self-organization throughout the perovskite. The vertical distribution behavior could arise from the coupling between hydrophilic and hydrophobic moieties in the D−π−A structure of TPA-FCA. The hydrophilic moieties of TPA-FCA with anchoring groups preferentially enable a fraction of molecules near the substrate side, while the hydrophobic moiety tends to diffuse toward the film surface as crystallization progresses. Therefore, this amphiphilic asymmetry drives a spontaneous vertical segregation of TPA-FCA, resulting in enrichment at both the bottom and top interfaces.

To capture the real-time crystallization dynamics of the perovskite films, we performed in situ photoluminescence (PL) and grazing-incidence wide-angle X-ray scattering (GIWAXS) measurements during spin-coating and subsequent annealing processes. The spin-coating process predominantly governs nucleation, and annealing mainly facilitates crystal growth.[15−17] As shown in Figure 1c,d, TPA-FCA can affect the nucleation-dominated crystallization process after antisolvent dripping, as evidenced by the reduced PL intensity. This behavior could be attributed to the strong interaction between TPA-FCA and perovskite, which slows down the nucleation rate.[16,17] In the following annealing process (Figure 1e,f), the initial stage reflects a competition between crystal growth and defect generation, leading to oscillations in PL intensity. As annealing proceeds, TPA-FCA is found to promote crystal growth, while the control film requires the prolonged time to reach the PL maximum. We further performed in situ GIWAXS to probe the structural and phase evolution during perovskite crystallization (Figure 1g). After the antisolvent dripping, the hexagonal 4H polycrystal phase (q = 8.4 nm^{-1}) emerges first and then transforms to the cubic 3C phase (q = 10.0 nm^{-1}).[18] The presence of TPA-FCA can accelerate this phase transformation and improve crystallinity, indicated by the evolution of diffraction intensity (Figure 1h). Collectively, these results demonstrate that TPA-FCA regulates both nucleation and subsequent crystal growth during perovskite crystallization.

The vertical segregation of the TPA-FCA ligand could favor perovskite growth from both interfaces toward the film center, leading to the bidirectional crystal growth of perovskite. Then, depth-dependent in situ GIWAXS was compared at 0.1° and 1°, which probe the top surface and deeper regions of the perovskite film, respectively (Figure S8). The distinct crystallization kinetic evolution observed at these two incident angles indicates that crystallization is initiated at both interfaces rather than proceeding exclusively from a single direction. The reduced time disparity of the maximum diffraction intensity suggests that TPA-FCA promotes more synchronous crystallization across the film thickness, consistent with a bidirectional growth scenario.

To understand the underlying mechanism, cellular automata (CA) models were developed to simulate the solidification of

https://doi.org/10.1021/jacs.6c02548
J. Am. Chem. Soc. 2026, 148, 13433−13443

perovskite solution and the dynamic behavior of ligands (more details can be found in the Supporting Information). Conventional perovskite growth is believed to proceed via two unidirectional scenarios: bottom-up (substrate to air) or top-down (air to substrate).[19] In both cases, large ligands tend to aggregate asymmetrically at one interface (Figure 2), which is against the experimentally observed distributional behaviors of TPA-FCA molecules. Thus, we propose an alternative bidirectional growth mechanism, wherein nucleation sites form at both the top (air/perovskite) and bottom (perovskite/substrate) interfaces in solution-processed perovskites.

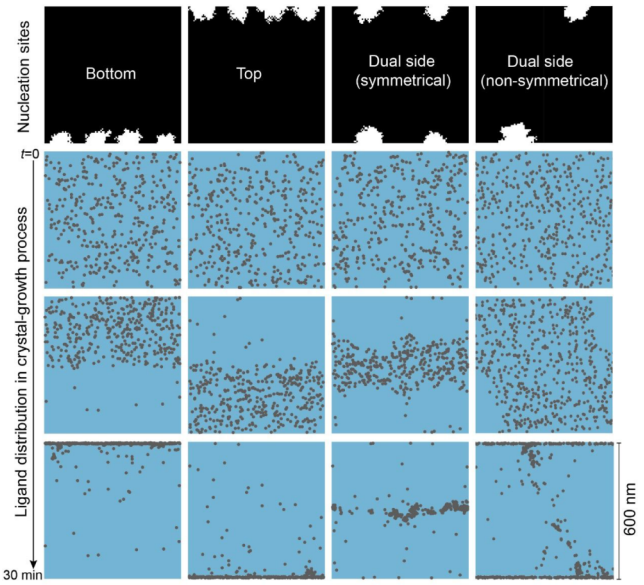

Figure 2. Cellular automata (CA) simulations for the nucleation and crystal-growth processes of perovskite. Note that the dark spots denote the ligand molecule.

According to classical nucleation theory, crystallization can proceed through homogeneous nucleation in a perovskite or heterogeneous nucleation at surfaces and interfaces. Because the nucleation barrier is reduced in the presence of interfaces, nucleation preferentially initiates at sites where the interfacial energy conditions are most favorable. This results in spatially inhomogeneous nucleation events near the substrate and the film−air interface. As discussed earlier, the D−π−A structure of TPA-FCA can further promote this behavior. Simulations of such a picture show ligand enrichment at both the top and bottom surfaces, consistent with our experimental observations. In turn, this dual-interface accumulation of TPA-FCA supports bidirectional growth: TPA-FCA is expelled from both advancing fronts and trapped as they converge (Video S1), accumulating at the two sides of the final films. Quantitative analysis further validates this ligand distribution pattern (Figure S9). In addition, if nucleation occurred perfectly symmetrically at both interfaces, ligands would accumulate at the midplane; however, this scenario is highly unlikely in real growth and inconsistent with our experimental observations.

Inspired by the most recent study,[11] such spontaneous bimodal distribution could modify the perovskite bulk and its heterointerfaces. The beneficial passivating TPA-FCA could mitigate the formation of defects during the crystallization arising from the polycrystalline and ionic nature of the perovskite.[20] Owing to its intrinsic ability to self-organize and

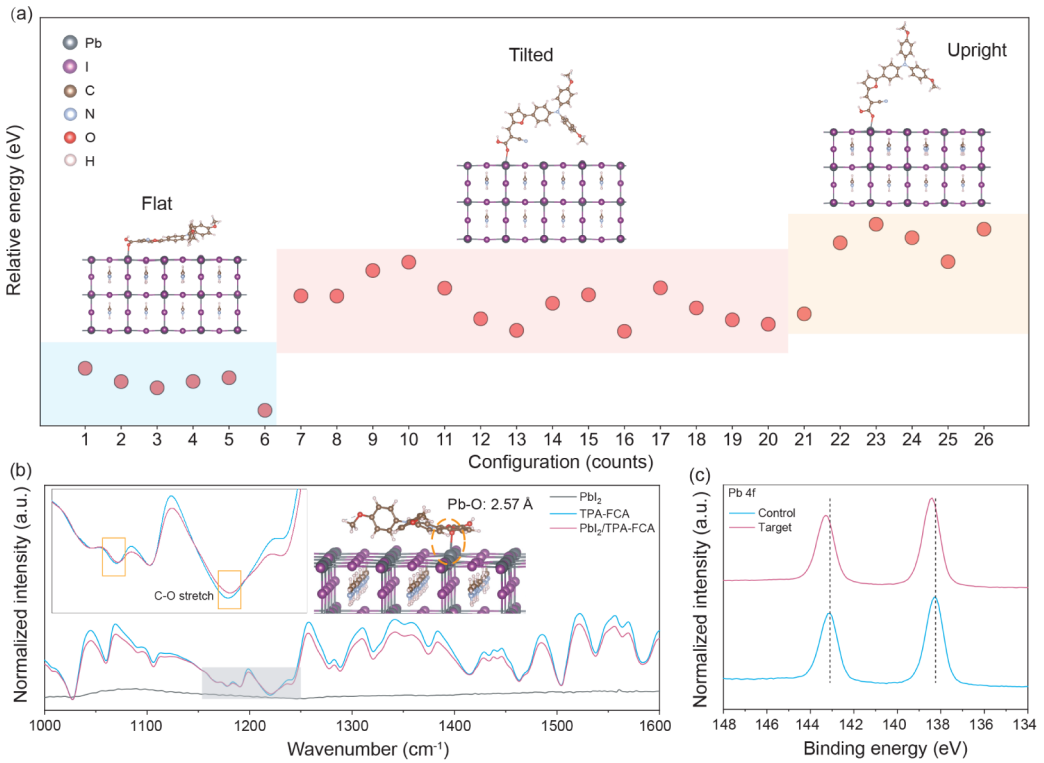

Figure 3. Interaction between TPA-FCA and perovskite. (a) Relative total energies of 26 configurations of TPA-FCA/$FAPbI_3$ (001), including flat (parallel to the surface), tilted (diagonal orientation), and upright (perpendicular). Note that the configuration 6 was referenced to zero. (b) FTIR spectra. The inset shows the detailed atomic structure of configuration 6. (c) High-resolution XPS of Pb 4f core-level spectra for perovskite film with or without TPA-FCA.

https://doi.org/10.1021/jacs.6c02548
J. Am. Chem. Soc. 2026, 148, 13433−13443

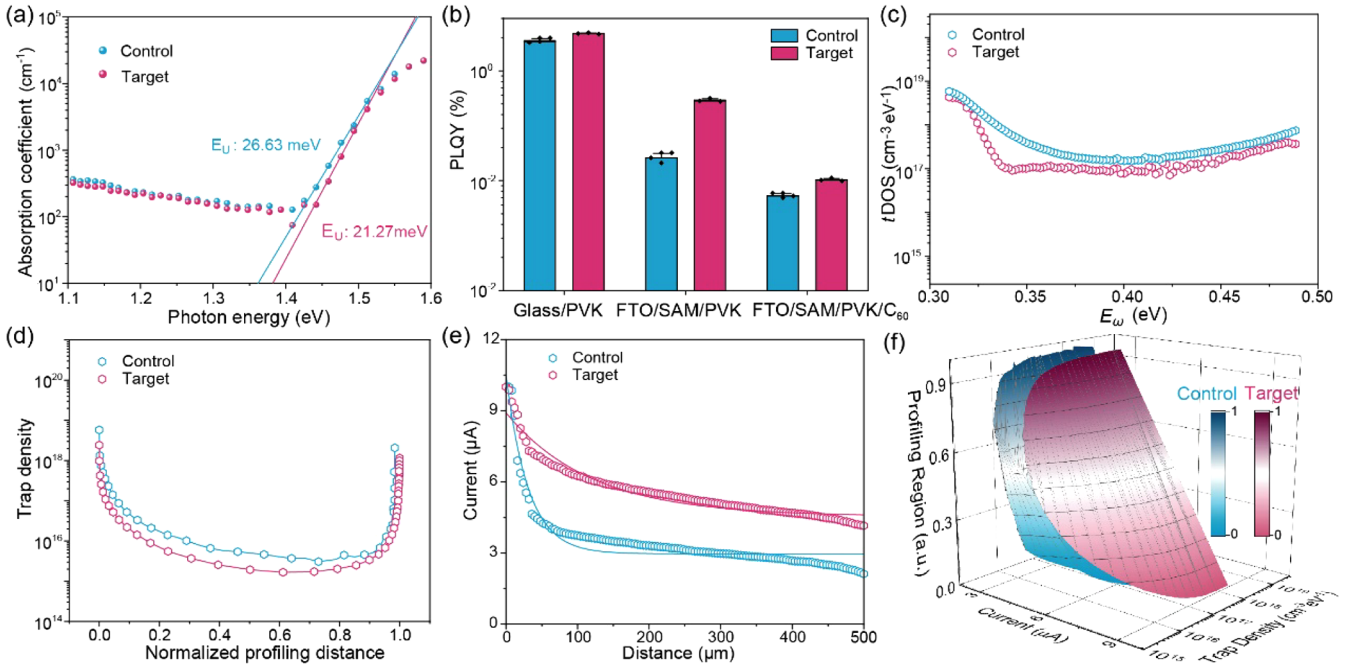

Figure 4. Defect characterizations of perovskite films and devices prepared with (target) and without (control) TPA-FCA. (a) PDS spectra of perovskite films. Note that all these films were deposited on quartz. (b) PLQY of perovskite films. PVK denotes perovskite. (c) Trap density of states (*t*DOS) obtained from thermal admittance spectroscopy. (d) Drive-level capacitance profiling (DLCP) curves. (e) Scanning photocurrent measurement system (SPMS) spectra of devices. (f) Integration of DLCP and SPMS data for trap density information in 3D space.

distribute regularly, TPA-FCA could further regulate the adjacent interfaces where the perovskite contacts the hole and electron transport layer, thereby delivering an "all-in-one" functionality.

Interaction Between TPA-FCA and Perovskite

The large-size structure could suppress TPA-FCA volatilization during perovskite annealing (see thermogravimetric analysis, TGA, in Figure S10), allowing the molecule to remain stable on the perovskite film surface.[21] To investigate this, we systematically explored the potential adsorption of TPA-FCA on the PbI_2-terminated $FAPbI_3$ (001) surface. As reported in previous work, molecules with multiple functional groups provide multiple binding motifs, enabling diverse adsorption configurations on the perovskite surface.[12] Given that TPA-FCA contains several functional groups, like a cyano group (−CN), a furan ring, and a carboxyl group, we constructed 26 configurations and did structural relaxation calculations (Figures S11 and S12). Three typical configurations, flat, tilted, and upright, are illustrated in Figure 3a. Relative total energy calculations show that the flat adsorption configuration is more stable than the other two, primarily because its larger interfacial contact area strengthens van der Waals interactions with the perovskite surface. Free-energy corrections were further applied to the adsorption energies of all configurations by including zero-point energy and vibrational entropy contributions at 300 K. The results show that the planar (flat) adsorption configuration remains the most stable among all considered geometries (Figure S13).

The most stable adsorption configuration is highlighted in Figure 3b, in which TPA-FCA and perovskite show a strong Pb−O interaction with a calculated bond length of 2.57 Å. Further calculated charge density difference (CDD) and effective Bader charge (Q_{eff}) analyses confirm the interfacial charge redistribution induced by Pb−O coordination (Figure S14). The CDD map exhibits a clear electron depletion region (blue) between the surface Pb site and the O atom, together with electron accumulation localized on the O atom. Consistently, the Pb site on the perovskite surface exhibits an increased positive charge (from 0.935 to 1.053 e), while the O atom of TPA-FCA becomes more negatively charged (from −1.063 to −1.144 e). Such an interaction was further studied by conducting attenuated total reflection-Fourier transform infrared (ATR-FTIR) and X-ray photoelectron spectroscopy (XPS). In FTIR spectra, the C−O stretching peaks in TPA-FCA at around 1180 cm^{-1} and 1220 cm^{-1} exhibit a shift to higher wavenumbers after contacting the perovskite main precursor of PbI_2. On the surface of the as-crystallized perovskite film, high-resolution XPS of the Pb 4f orbital (Figure 3c, Figure S15), including Pb 4f 7/2 and Pb 4f 5/2 orbitals, shifted to higher binding energies for the TPA-FCA-containing film. These observations confirm the coordination interaction between TPA-FCA and Pb^{2+}. As DFT calculations suggested, the oxygen atom from the COOH group in TPA-FCA forms a Pb−O bond with perovskite. This interaction can change the local electron density distribution in perovskite, leading to electron withdrawal from the Pb−I bonds. As a result, Pb becomes increasingly electron-deficient, leading to an increase in the binding energies.[22] The redistribution of the electrons at the molecule-perovskite interface could influence the optical properties of perovskites.

While TPA-FCA does not significantly alter the light absorption and optical bandgap (Figure S16), it will improve the photoluminescence (PL) of the perovskite film. On different bottom contacts, the TPA-FCA-containing films show enhanced absolute PL intensities (Figure S17), with even over a 3-fold increase compared to the control film when depositing on the self-assembled materials (SAM)-coated substrate. These improvements could originate from the special structure of TPA-FCA. Since the SAM normally

https://doi.org/10.1021/jacs.6c02548
J. Am. Chem. Soc. 2026, 148, 13433−13443

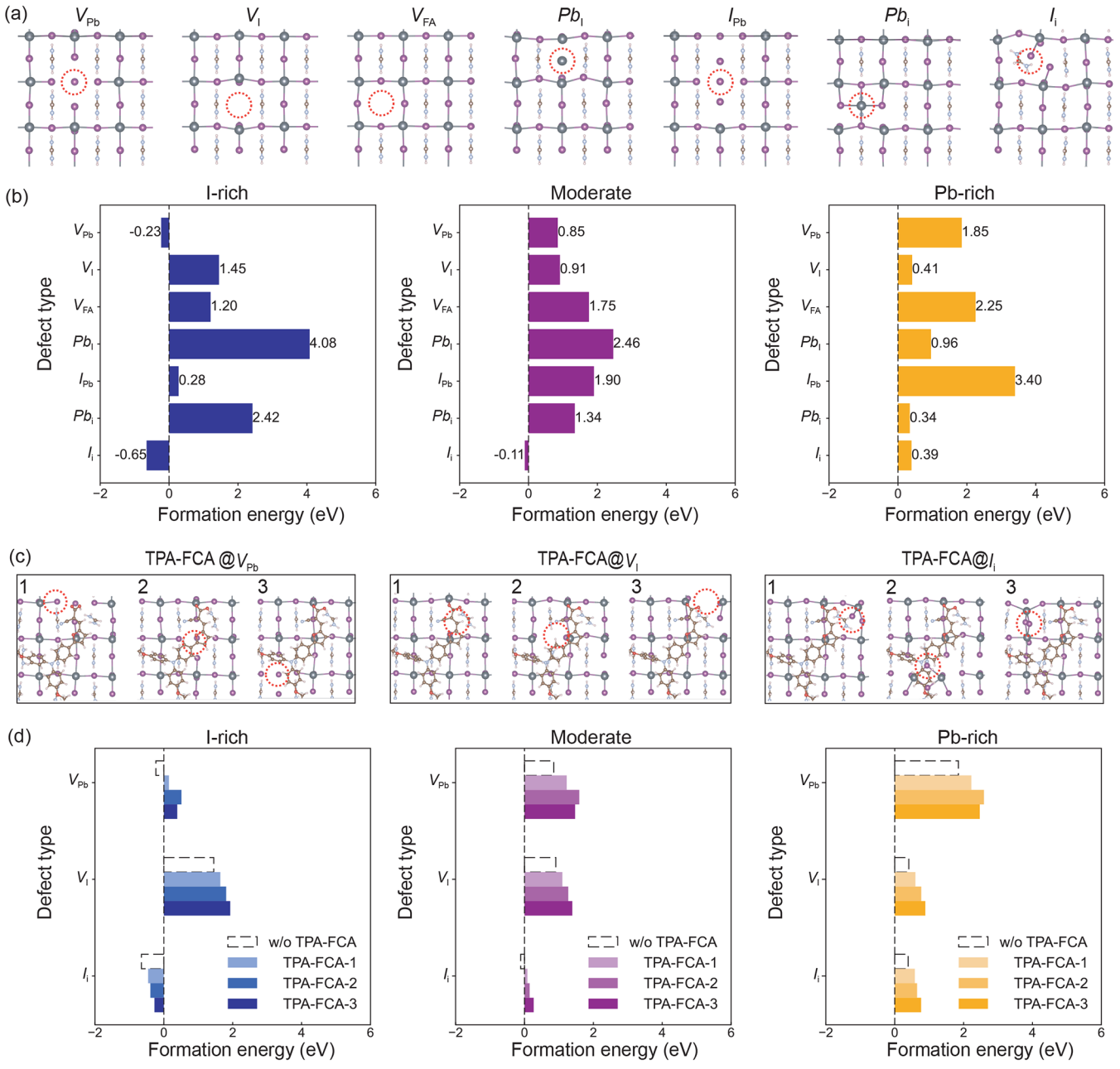

Figure 5. Configurations and formation energy variations of surface defects in $FAPbI_3$ without and with TPA-FCA adsorption. (a) Schematics of the seven defect types: three vacancies (V_{Pb}, V_I, V_{FA}), two antisites (Pb_I, I_{Pb}) and two interstitials (Pb_i, I_i), marked by red circles. (b) Defect formation energies without TPA-FCA adsorption under the I-rich, moderate, and Pb-rich conditions. (c) Top views of TPA-FCA adsorption around V_{Pb}, V_I, and I_i defects (highlighted by red circles). Here, we considered three adsorption configurations marked as 1, 2, and 3. (d) Formation energies of V_{Pb}, V_I, and I_i with TPA-FCA adsorption under different growth conditions. Note that the black dashed rectangles indicate the reference defect formation energies without TPA-FCA adsorption, while others present those with adsorption.

encounters nonuniform coating at the bottom interface,[23] TPA-FCA could offer a complementary function thanks to its anchoring groups, which form covalent or hydrogen bonding with the bottom substrate.[12] This characteristic will fill the uncovered SAM hole transporter, contributing to better crystallinity of perovskite films, evidenced by the enhanced ratio of (100)/(110) facet orientations (Figure S5). Photothermal deflection spectroscopy (PDS) spectra show that the TPA-FCA can lower the Urbach energy (E_u) of the perovskite film (Figure 4a), indicating the reduced band edge disorder.[24] This reduction is expected to suppress subgap trap-assisted recombination, thereby enhancing the PL quantum yield (PLQY). Further calculation of PLQY confirmed the suppression of nonradiative recombination after introduction of TPA-FCA (Figure 4b).

As the recombination loss could happen in both the perovskite bulk and its adjacent interfaces in the complete solar cells, our self-organizing TPA-FCA could act as a passivating ligand to spatially interact with defects. We first conducted the thermal admittance spectroscopy (TAS) to quantify trap states in the devices.[25] The energetic distribution of the trap density of states (*t*DOS) is presented in Figure 4c. Following TPA-FCA modification, a reduction in both shallow-level (Band I, 0.31−0.4 eV) and deep-level traps

https://doi.org/10.1021/jacs.6c02548
J. Am. Chem. Soc. 2026, 148, 13433−13443

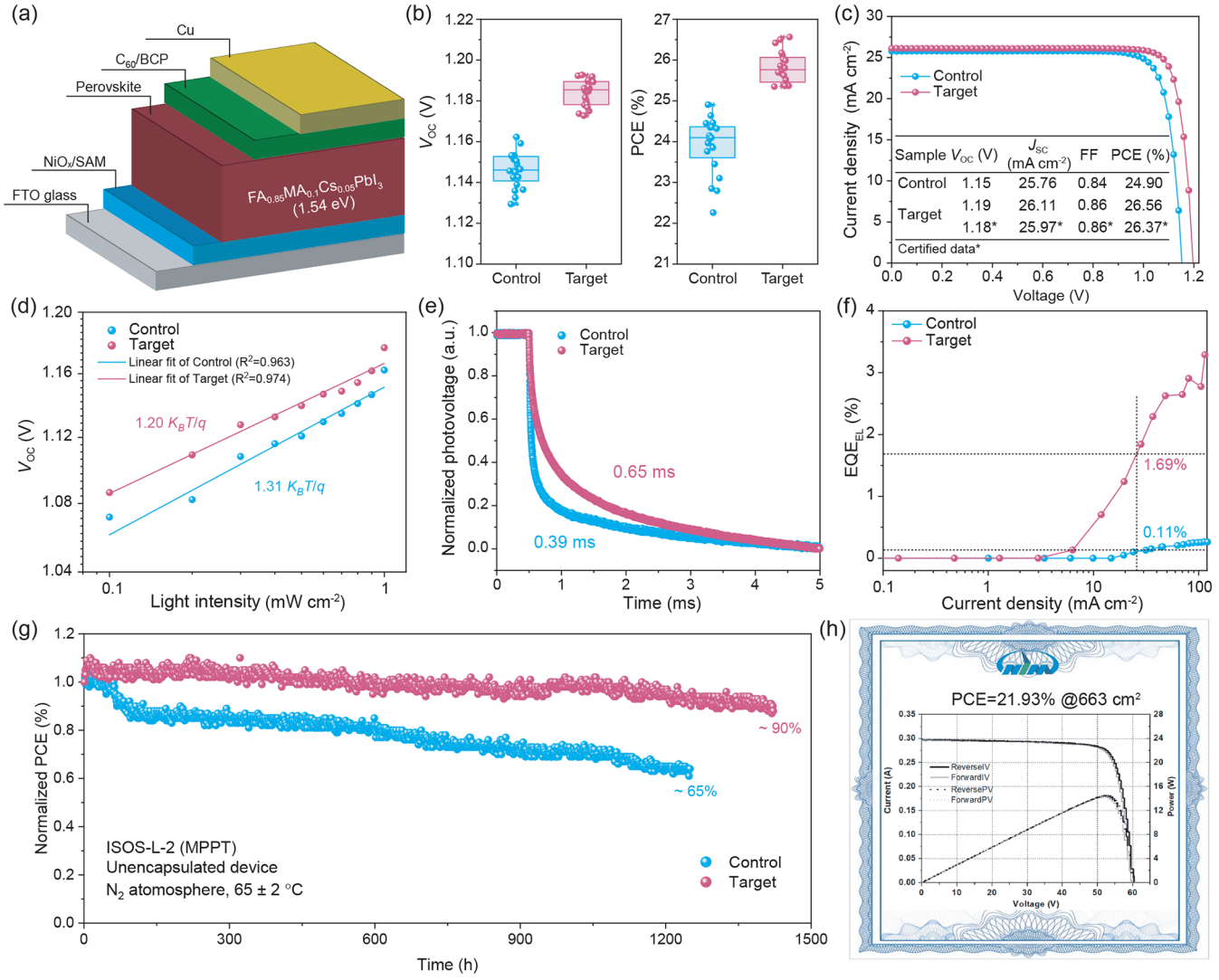

Figure 6. Photovoltaic performance of inverted perovskite solar cells. (a) Schematic device structure. (b) Statistical distributions of photovoltaic parameters (V_{OC}, J_{SC}, FF, and PCE). The data shown here were collected from 20 devices. (c) J–V curves of the champion device obtained from the reverse scan (RS, 1.2 to −0.2 V). (d) Light intensity-dependent V_{OC}. For each point, the data were obtained from the reverse scan. (e) TPV decay curves. (f) EQE of EL spectra. (g) Long-term operational stability under maximum power point tracking. The initial PCEs of control and target devices are around 24.5% and 25.6%, respectively. (h) Certified I-V curves for the perovskite module based on the TPA-FCA modification. Note that the aperture area is 663 cm^2.

(Band II and III, >0.4 eV) was observed. Then, drive-level capacitance profiling (DLCP) was performed to study the spatial distribution of defects. The far-end curve in Figure 4d corresponds to the interfaces, with the left end representing the top interface and the right end corresponding to the buried interface. These interfacial regions exhibit higher defect densities compared to the perovskite bulk, consistent with previous reports.[7] Remarkably, the introduction of TPA-FCA effectively suppressed trap states not only within the bulk but also at both interfaces. Furthermore, scanning photocurrent measurement system (SPMS) analysis revealed an increased carrier diffusion length in the TPA-FCA-modified device, indicating a lower density of trap states across the perovskite surface (Figure 4e).[26] By integrating DLCP and SPMS (or *t*DOS and SPMS in Figure S18), a reconstructed spatial visualization of trap state distribution was achieved, as depicted in Figure 4f. The three-dimensional profile demonstrates uniformly reduced trap state densities and enhanced photocurrent values throughout the TPA-FCA-treated device,[27] providing clear evidence of effective defect passivation at both the interfaces and in the bulk region. Therefore, these multidisciplinary characterizations consistently affirm the comprehensive passivation effect achieved by self-organizing TPA-FCA molecules.

To gain insight into the nature of defect passivation, we investigated seven types of surface defects in Figure 5a, including three vacancies (V_{Pb}, V_I, V_{FA}), two antisites (Pb_I, I_{Pb}), and two interstitials (Pb_i, I_i). Since the growth condition influences the defect formation, Figure 5b presents the formation energies of these defects under I-rich (Pb-poor), moderate, and Pb-rich (I-poor) conditions (Figure S19).[28,29] Among them, V_{Pb}, V_I, and I_i are identified as representative defects due to their distinct formation energy profiles. Given the established passivation effect of TPA-FCA, we further examined the impact of TPA-FCA adsorption on the formation of these defects. The adsorbed TPA-FCA molecule alters the local surface environment near the adsorption site, which, in turn, affects the defect formation energy. To capture these

https://doi.org/10.1021/jacs.6c02548
J. Am. Chem. Soc. 2026, 148, 13433−13443

variations, each defect type was positioned at three sites close to the molecule adsorbed (Figure 5c). The corresponding formation energies of these defect configurations are summarized in Figure 5d. The defect formation energies are higher in the presence of TPA-FCA adsorption than in its absence under all the growth conditions, suggesting that TPA-FCA stabilizes the lattice and suppresses the defect formation in the final perovskite, consistent with the experimental results.

The influence of adjacent charge-transport layers (C_{60} and NiO_x) on the adsorption configuration of TPA-FCA was evaluated by DFT calculations. For the C_{60} layer, three representative initial configurations were constructed (Figure S20a), all of which relax to the same planar adsorption geometry of TPA-FCA on the perovskite surface, indicating that C_{60} does not perturb the adsorption configuration. For the NiO_x layer, three initial models with TPA-FCA/NiO separations of 1.30, 1.70, and 2.20 Å were considered. After structural relaxation (Figure S20b), the adsorption geometry of TPA-FCA remains unchanged in all cases, while the optimized separations increase to 2.12−2.37 Å, suggesting weak interactions between TPA-FCA and NiO_x that do not alter the intrinsic adsorption configuration.

Additionally, given that the large-size π-conjugated organic ligands could also induce the 2D perovskite on the surface,[30] we thus conducted ex situ surface-sensitive GIWAXS measurements. There is no 2D signal that can be detected from the surface of the 3D perovskite (Figure S21), confirming the TPA-FCA ligand passivation mainly due to the molecular function rather than the 2D/3D heterojunction engineering. Therefore, we mainly utilized the self-organizing effect of our TPA-FCA. The resulting interfacial localization at both charge-extracting contacts likely contributes to reduced nonradiative recombination losses and improved overall device performance.

Photovoltaic Performance and Stability of TPA-FCA-containing Device

Building on the characteristics of TPA-FCA, we fabricated the inverted PSCs as illustrated in Figure 6a, with a structure of glass/FTO/NiO_x/SAM/perovskite/C_{60}/BCP/Cu. Detailed device fabrication can be found in the experimental sections, and the optimization process of TPA-FCA is shown in Figure S22. The 3D ToF-SIMS depth profiling of the complete device reveals a dual-side distribution of TPA-FCA within the perovskite layer (Figure S23), directly validating the necessity of the D−π−A molecular architecture for the effective regulation of both interfaces. Compared to the control, the TPA-FCA-containing devices show improved PCEs from 23.92 ± 0.69 to 25.82 ± 0.39% (arithmetic mean ± standard deviation), mainly contributed by the open-circuit voltage (V_{OC}) from 1.15 ± 0.01 to 1.18 ± 0.01 V and fill factor (FF) from 0.82 ± 0.02 to 0.85 ± 0.01 (Figure 6b). These increased V_{OC} and FF values are consistent with the passivation effect. The average short-circuit current density (J_{SC}) shows similar values, 25.48 ± 0.28 mA cm^{-2} and 25.68 ± 0.33 mA cm^{-2}, respectively, indicating the TPA-FCA cannot impair the light absorption or slow charge transfer at the interface, likely owing to its π-conjugated bridge structure.[11] The integrated J_{SC} from the external quantum efficiency (EQE) spectrum matched well with the J_{SC} obtained from the J−V measurements (Figure S24). Encouragingly, TPA-FCA boosts the champion PCEs from 24.90 to 26.56% (Figure 6c). We also sent one of the devices to an independently accredited laboratory (Figure S25). The best-performing device shows a certified PCE of 26.37% (V_{OC} = 1.18 V, J_{SC} = 25.97 mA cm^{-2}, and FF = 0.86), confirming the reliability of our lab-measured data. Beyond the normal-bandgap composition, we further applied our strategy to a wide-bandgap (1.68 eV) perovskite. Devices incorporating TPA-FCA deliver enhanced performance, suggesting the applicability of this approach across different perovskite bandgaps (Figure S26).

To understand the mechanism of performance improvements, we conducted a series of in-depth characterizations. From 0.1 to 1 Sun, light-intensity-dependent J−V measurements were performed continuously (Figure S27). The TPA-FCA-modified devices exhibit a higher FF compared to the control at various light intensities, suggesting improved charge extraction and reduced carrier recombination under operational conditions. To understand the FF improvement, we analyze the FF losses in the complete devices.[31] When they behave as an ideal diode, the maximum FFs of the control and TPA-FCA-containing devices are 0.87 and 0.88, respectively (Figure S28, Note S1). After considering parasitic resistance, the calculated FFs are 0.81 and 0.84 for the control and target devices. The total FF loss decreased from 0.09 to 0.06, indicating the effectiveness of the approach in this study. Therefore, TPA-FCA is beneficial to reduce both nonradiative and charge-transport losses. Since the perpendicular binding is reported to produce dense packing and introduce an unwanted resistance on the perovskite surface,[6] the reduced charge-transport losses are mainly due to the flat adsorption of our TPA-FCA, as discussed earlier.

Additionally, J_{SC} and V_{OC} increase monotonically with illumination intensity, consistent with standard photogeneration behavior in high-performance PSCs. The dominant recombination mechanism was analyzed by examining the V_{OC} dependence on light intensity, from which the ideality factor can be extrapolated.[32] The TPA-FCA-modified device exhibits an ideality factor of 1.20, compared to 1.31 for the control (Figure 6d). Given that the lower ideality factor typically indicates a reduced contribution from trap-assisted (Shockley−Read−Hall) recombination,[33] the introduction of TPA-FCA can significantly suppress the nonradiative recombination. Further transient photovoltage (TPV) measurements were conducted as shown in Figure 6e. The longer TPV decay time (0.65 vs 0.39 ms) after introducing TPA-FCA confirmed the reduced recombination losses owing to effective passivation of interfacial and bulk trap states by the multifunctional TPA-FCA ligand, as discussed above. Kelvin probe force microscopy (KPFM) measurements on the top surface of the perovskite film show a shift in the contact potential difference toward more n-type behavior (Figure S29), indicating efficient electron transport in the final devices. The charge transport dynamics are further studied by transient photocurrent (TPC) and electrochemical impedance spectroscopy (EIS) measurements. The time constant derived from TPC decreases from 0.46 to 0.35 μs, indicating reduced carrier recombination and enhanced carrier transport in the target device (Figure S30). This is further demonstrated by the increased recombination resistance (R_{rec}) from 8590 to 13917 Ω in the EIS fitting parameters (Figure S31).

To further quantify the energy losses, we calculated the $\Delta V_{OC,nrad}$ (nonradiative V_{OC} loss) based on the external quantum efficiency of electroluminescence (EQE_{EL}).[34] When operating as light-emitting diodes (LEDs), the EL spectra of TPA-FCA devices show higher intensities than those of the

https://doi.org/10.1021/jacs.6c02548
J. Am. Chem. Soc. 2026, 148, 13433−13443

control (Figure S32). At a bias of 1.8 V, the EL emission of TPA-FCA devices is observed to be much stronger (over 30 times) than the control device. At 1-sun equivalent current injection (~25 mA cm^{-2}), the EQE_{EL} of the TPA-FCA device is 1.69%, while the control device is only 0.11% (Figure 6f). Following the equation of $\Delta V_{OC,nrad} = -k_B T/q \ln(EQE_{EL})$, where k_B is the Boltzmann constant, T is the temperature, and q is the elementary charge, we calculated the $\Delta V_{OC,nrad}$ of the TPA-FCA device to be 0.105 V, which is lower than that of the control device (0.176 V). This reduction further confirms the suppressed energy losses of the TPA-FCA-containing device.

The reduced trap-state-driven nonradiative recombination can not only improve the performance but more significantly the device stability.[20,35] The operational stressors, like the interplay of light, heat, and bias, can further accelerate the trap accumulation and migration of the charged defects, inducing faster degradation under operational conditions. To evaluate the stability of the PSCs, we adopted the standard protocols based on the statements of the International Summit on Organic Photovoltaic Stability (ISOS).[36] Under continuous maximum power point tracking at 65 °C (ISOS-L-2), the TPA-FCA-containing device shows an improved stability, with the unencapsulated device still maintaining around 90% of its initial efficiency after 1400 h (Figure 6g). By contrast, the control device lost over 30% after a shorter period of 1200 h, with a clear rapid degradation in the initial stage (~100 h, also known as the burn-in effect). Given that this burn-in effect is related to the perovskite quality and the interfaces between perovskite and charge transport layers,[37] the enhanced operational stability confirmed that our self-organizing TPA-FCA can simultaneously manipulate both the perovskite bulk and adjacent heterointerfaces.

Furthermore, self-organizing TPA-FCA can reduce or even eliminate the need for additional passivation agents. This simplification of the fabrication process is particularly advantageous for large-area perovskite modules. By unifying bulk and interface passivation within a single molecular framework, TPA-FCA could provide a more controlled, reliable, and scalable strategy for high-performance PSCs. To validate its scalability, we fabricated 30 cm × 30 cm perovskite modules incorporating the bifunctional TPA-FCA. The champion module exhibits negligible hysteresis in the $I-V$ curves (Figure 6h, Figure S33), with a V_{OC} of 59.93 V, an I_{SC} of 0.297 A, an FF of 0.80, and a PCE of 21.59% in the forward scan and a V_{OC} of 60.41 V, an I_{SC} of 0.299 A, an FF of 0.80, and a PCE of 21.93% in the reverse scan. These results highlight the excellent scalability of TPA-FCA for large-area perovskite photovoltaics.

CONCLUSION

In summary, we uncover the self-organizing behavior of TPA-FCA and its dual-interface passivation mechanism during perovskite crystallization. This D−π−A ligand effectively suppresses bulk and interfacial defects (e.g., V_{Pb}, V_I, and I_i), thereby reducing nonradiative recombination and charge-transport losses. Consequently, TPA-FCA enables PSCs with a champion efficiency of 26.56% (26.37% certified on 0.0653 cm^2) and scalable modules with a champion efficiency of 21.93% (certified on 663 cm^2) together with outstanding operational stability, retaining 90% of the initial performance after 1400 h under continuous operation. This work establishes molecular self-organization as a robust strategy for designing multifunctional ligands that unite efficiency, stability, and scalability in perovskite photovoltaics.

ASSOCIATED CONTENT

Supporting Information

The Supporting Information is available free of charge at https://pubs.acs.org/doi/10.1021/jacs.6c02548.

Materials, experimental methods, and additional characterizations, such as DFT calculations, ^{1}H NMR, DLS, XRD, SEM, ToF-SIMS, CA, TGA, XPS, UV−vis, TPC, EIS, device statistics, and certification reports (PDF)

Dynamic nucleation and crystal growth in perovskite films simulated by CA (MP4)

AUTHOR INFORMATION

Corresponding Authors

Qing Lian − *Department of Materials Science and Engineering, Southern University of Science and Technology, Shenzhen, Guangdong 518055, China; College of Engineering and Design, Hunan Normal University, Changsha 410081, China*; Email: lianq@hunnu.edu.cn

Yan-Fang Zhang − *School of Physical Sciences, University of Chinese Academy of Sciences, Beijing 100049, China*; Email: zhangyanfang@ucas.ac.cn

Yanming Wang − *Future Photovoltaic Research Center, Global Institute of Future Technology, Shanghai Jiao Tong University, Shanghai 200240, China*; orcid.org/0000-0002-0912-681X; Email: yanming.wang@sjtu.edu.cn

Xugang Guo − *Department of Materials Science and Engineering, Southern University of Science and Technology, Shenzhen, Guangdong 518055, China*; orcid.org/0000-0001-6193-637X; Email: guoxg@sustech.edu.cn

Yixin Zhao − *Future Photovoltaic Research Center, Global Institute of Future Technology, Shanghai Jiao Tong University, Shanghai 200240, China; School of Environmental Science and Engineering, Frontiers Science Center for Transformative Molecules and State Key Laboratory of Green Papermaking and Resource Recycling, Shanghai Jiao Tong University, Shanghai 200240, China; Shanghai Non-carbon Energy Conversion and Utilization Institute, Shanghai 200240, China*; orcid.org/0000-0002-8663-9993; Email: yixin.zhao@sjtu.edu.cn

Authors

Bowei Li − *Future Photovoltaic Research Center, Global Institute of Future Technology, Shanghai Jiao Tong University, Shanghai 200240, China; Shanghai Non-carbon Energy Conversion and Utilization Institute, Shanghai 200240, China*

Yahong Pu − *Beijing National Laboratory for Condensed Matter Physics, Institute of Physics, Chinese Academy of Sciences, Beijing 100190, China; School of Physical Sciences, University of Chinese Academy of Sciences, Beijing 100049, China*

Chi Chen − *Future Photovoltaic Research Center, Global Institute of Future Technology, Shanghai Jiao Tong University, Shanghai 200240, China*; orcid.org/0009-0005-2154-1986

Jing Chen − *Institute of Functional Nano & Soft Materials (FUNSOM), Jiangsu Key Laboratory of Advanced Negative Carbon Technologies, Soochow University, Suzhou 215123, China*

Zhixiao Qin − *Shanghai Pvsktech Co., Ltd., Shanghai 201109, China*
Wenji Zhan − *School of Environmental Science and Engineering, Frontiers Science Center for Transformative Molecules, Shanghai Jiao Tong University, Shanghai 200240, China*
Chujun Zhang − *Hunan Key Laboratory for Super-microstructure and Ultrafast Process, School of Physics, Central South University, Changsha 410083, China*
Zhenhuang Su − *Shanghai Synchrotron Radiation Facility, Shanghai Advanced Research Institute, Shanghai Institute of Applied Physics Chinese Academy of Sciences, Shanghai 201204, China;* orcid.org/0000-0003-0026-2601
Jiahao Guo − *School of Environmental Science and Engineering, Frontiers Science Center for Transformative Molecules, Shanghai Jiao Tong University, Shanghai 200240, China*
Bin Liu − *Department of Materials Science and Engineering, Southern University of Science and Technology, Shenzhen, Guangdong 518055, China*
Jiasheng Su − *Future Photovoltaic Research Center, Global Institute of Future Technology, Shanghai Jiao Tong University, Shanghai 200240, China*
Anran Yu − *Center of Micro-Nano System, School of Information Science and Technology, Fudan University, Shanghai 200438, China;* orcid.org/0009-0009-4621-557X
Yu Zou − *Future Photovoltaic Research Center, Global Institute of Future Technology, Shanghai Jiao Tong University, Shanghai 200240, China;* orcid.org/0000-0002-4413-1139
Yao Wang − *Future Photovoltaic Research Center, Global Institute of Future Technology, Shanghai Jiao Tong University, Shanghai 200240, China; Shanghai Non-carbon Energy Conversion and Utilization Institute, Shanghai 200240, China*
Yuetian Chen − *School of Environmental Science and Engineering, Frontiers Science Center for Transformative Molecules, Shanghai Jiao Tong University, Shanghai 200240, China; Shanghai Non-carbon Energy Conversion and Utilization Institute, Shanghai 200240, China;* orcid.org/0000-0003-3516-8199
Yanfeng Miao − *School of Environmental Science and Engineering, Frontiers Science Center for Transformative Molecules, Shanghai Jiao Tong University, Shanghai 200240, China; Shanghai Non-carbon Energy Conversion and Utilization Institute, Shanghai 200240, China*
Junliang Yang − *Hunan Key Laboratory for Super-microstructure and Ultrafast Process, School of Physics, Central South University, Changsha 410083, China;* orcid.org/0000-0002-5553-0186
Yiqiang Zhan − *Center of Micro-Nano System, School of Information Science and Technology, Fudan University, Shanghai 200438, China;* orcid.org/0000-0001-8391-2555
Zhao-Kui Wang − *Institute of Functional Nano & Soft Materials (FUNSOM), Jiangsu Key Laboratory of Advanced Negative Carbon Technologies, Soochow University, Suzhou 215123, China;* orcid.org/0000-0003-1707-499X
Anlian Pan − *School of physics and electronics, Hunan Normal University, Changsha 410081, China;* orcid.org/0000-0003-3335-3067
Shixuan Du − *Beijing National Laboratory for Condensed Matter Physics, Institute of Physics, Chinese Academy of Sciences, Beijing 100190, China; School of Physical Sciences, University of Chinese Academy of Sciences, Beijing 100049, China;* orcid.org/0000-0001-9323-1307

Complete contact information is available at: https://pubs.acs.org/10.1021/jacs.6c02548

Author Contributions

△B.L., Y.P., C.C., J.C., and Z.Q. contributed equally to this work.

Notes

The authors declare no competing financial interest.

■ ACKNOWLEDGMENTS

The authors gratefully acknowledge the financial support by the National Natural Science Foundation of China (NSFC, Grant Nos. 22025505, 22220102002, 52203334, 22522903, 22305111, 52403330, and 22409130), Natural Science Foundation of Shanghai (Grant Nos. 23ZR1432300 and 23ZR1428000), Shanghai Science and Technology Innovation Action Plan (24DZ3001203), Shenzhen Science and Technology Innovation Program (KCXST20221021111413031), Shanghai Science and Technology Commission Program (25DZ3001902), Shanghai Jiao Tong University 2030 Initiative (Grant No. WH510363004/003), and Startup Fund for Young Faculty at SJTU (SFYF at SJTU, 24X010502888). We acknowledge the BL14B1 beamline of the Shanghai Synchrotron Radiation Facility (SSRF) for assistance with GIWAXS measurement and the Instrumental Analysis Center of Shanghai Jiao Tong University and the School of Environmental Science and Engineering for assistance with characterizations. B.L. thanks H. Yang, T. Zhu, and S. Hong from Shanghai Ideaoptics Co., Ltd. for kind assistance in PLQY measurements and Hunan Nanoup Electronics Technology Co., Ltd. for PDS measurements.

■ REFERENCES

(1) Zhang, L.; Mei, L.; Wang, K.; Lv, Y.; Zhang, S.; Lian, Y.; Liu, X.; Ma, Z.; Xiao, G.; Liu, Q.; et al. Advances in the Application of Perovskite Materials. *Nano-Micro Lett.* **2023**, *15* (1), 177.
(2) Stranks, S. D.; Snaith, H. J. Metal-Halide Perovskites for Photovoltaic and Light-Emitting Devices. *Nat. Nanotechnol.* **2015**, *10* (5), 391−402.
(3) NREL *Best Research-Cell Efficiencies*. https://www.nrel.gov/pv/assets/pdfs/b-est-research-cell-efficiencies.pdf. (accessed: December 2025).
(4) Li, C.; Wang, X.; Bi, E.; Jiang, F.; Park, S. M.; Li, Y.; Chen, L.; Wang, Z.; Zeng, L.; Chen, H.; Liu, Y.; Grice, C. R.; Abudulimu, A.; Chung, J.; Xian, Y.; Zhu, T.; Lai, H.; Chen, B.; Ellingson, R. J.; Fu, F.; Ginger, D. S.; Song, Z.; Sargent, E. H.; Yan, Y. Rational Design of Lewis Base Molecules for Stable and Efficient Inverted Perovskite Solar Cells. *Science* **2023**, *379* (6633), 690−694.
(5) Park, S. M.; Wei, M.; Xu, J.; Atapattu, H. R.; Eickemeyer, F. T.; Darabi, K.; Grater, L.; Yang, Y.; Liu, C.; Teale, S.; Chen, B.; Chen, H.; Wang, T.; Zeng, L.; Maxwell, A.; Wang, Z.; Rao, K. R.; Cai, Z.; Zakeeruddin, S. M.; Pham, J. T.; Risko, C. M.; Amassian, A.; Kanatzidis, M. G.; Graham, K. R.; Grätzel, M.; Sargent, E. H. Engineering Ligand Reactivity Enables High-Temperature Operation of Stable Perovskite Solar Cells. *Science* **2023**, *381* (6654), 209−215.
(6) Chen, H.; Liu, C.; Xu, J.; Maxwell, A.; Zhou, W.; Yang, Y.; Zhou, Q.; Bati, A. S. R.; Wan, H.; Wang, Z.; Zeng, L.; Wang, J.; Serles, P.; Liu, Y.; Teale, S.; Liu, Y.; Saidaminov, M. I.; Li, M.; Rolston, N.; Hoogland, S.; Filleter, T.; Kanatzidis, M. G.; Chen, B.; Ning, Z.;

Sargent, E. H. Improved Charge Extraction in Inverted Perovskite Solar Cells with Dual-Site-Binding Ligands. *Science* **2024**, *384* (6692), 189−193.
(7) Ni, Z.; Bao, C.; Liu, Y.; Jiang, Q.; Wu, W. Q.; Chen, S.; Dai, X.; Chen, B.; Hartweg, B.; Yu, Z.; Holman, Z.; Huang, J. Resolving Spatial and Energetic Distributions of Trap States in Metal Halide Perovskite Solar Cells. *Science* **2020**, *367* (6484), 1352−1358.
(8) Li, B.; Xiang, Y.; Jayawardena, K. D. G. I.; Luo, D.; Watts, J. F.; Hinder, S.; Li, H.; Ferguson, V.; Luo, H.; Zhu, R.; et al. Tailoring Perovskite Adjacent Interfaces by Conjugated Polyelectrolyte for Stable and Efficient Solar Cells. *Sol. RRL* **2020**, *4*, 2000060.
(9) Zhang, Y.; Wang, Y.; Zhao, L.; Yang, X.; Hou, C. H.; Wu, J.; Su, R.; Jia, S.; Shyue, J. J.; Luo, D.; Chen, P.; Yu, M.; Li, Q.; Li, L.; Gong, Q.; Zhu, R. Depth-Dependent Defect Manipulation in Perovskites for High-Performance Solar Cells. *Energy Environ. Sci.* **2021**, *14* (12), 6526−6535.
(10) Zhou, Y.; Game, O. S.; Pang, S.; Padture, N. P. Microstructures of Organometal Trihalide Perovskites for Solar Cells: Their Evolution from Solutions and Characterization. *J. Phys. Chem. Lett.* **2015**, *6* (23), 4827−4839.
(11) Lian, Q.; Wang, L.; Wang, G.; Mi, G.; Li, B.; Smith, J. A.; Caprioglio, P.; Kober-Czerny, M.; Wang, D.; Yin, Q.; et al. Dual Molecular Bridges at Perovskite Heterointerfaces for Efficient Inverted Solar Cells. *Natl. Sci. Rev.* **2025**, *12* (7), nwaf211.
(12) Zhang, S.; Wu, R.; Mu, C.; Wang, Y.; Han, L.; Wu, Y.; Zhu, W. H. Conjugated Self-Assembled Monolayer as Stable Hole-Selective Contact for Inverted Perovskite Solar Cells. *ACS Mater. Lett.* **2022**, *4* (10), 1976−1983.
(13) Peng, J.; Khan, J. I.; Liu, W.; Ugur, E.; Duong, T.; Wu, Y.; Shen, H.; Wang, K.; Dang, H.; Aydin, E.; et al. A Universal Double-Side Passivation for High Open-Circuit Voltage in Perovskite Solar Cells: Role of Carbonyl Groups in Poly(Methyl Methacrylate). *Adv. Energy Mater.* **2018**, *8* (30), 1801208.
(14) Zhang, S.; Ye, F.; Wang, X.; Chen, R.; Zhang, H.; Zhan, L.; Jiang, X.; Li, Y.; Ji, X.; Liu, S.; Yu, M.; Yu, F.; Zhang, Y.; Wu, R.; Liu, Z.; Ning, Z.; Neher, D.; Han, L.; Lin, Y.; Tian, H.; Chen, W.; Stolterfoht, M.; Zhang, L.; Zhu, W. H.; Wu, Y. Minimizing Buried Interfacial Defects for Efficient Inverted Perovskite Solar Cells. *Science* **2023**, *380* (6643), 404−409.
(15) Huang, T.; Tan, S.; Nuryyeva, S.; Yavuz, I.; Babbe, F.; Zhao, Y.; Abdelsamie, M.; Weber, M. H.; Wang, R.; Houk, K. N.; et al. Performance-Limiting Formation Dynamics in Mixed-Halide Perovskites. *Sci. Adv.* **2021**, *7* (46), No. eabj1799.
(16) Yang, T.; Ma, C.; Cai, W.; Wang, S.; Wu, Y.; Feng, J.; Wu, N.; Li, H.; Huang, W.; Ding, Z.; et al. Amidino-Based Dion-Jacobson 2D Perovskite for Efficient and Stable 2D/3D Heterostructure Perovskite Solar Cells. *Joule* **2023**, *7* (3), 574−586.
(17) An, Y.; Zhang, N.; Zeng, Z.; Cai, Y.; Jiang, W.; Qi, F.; Ke, L.; Lin, F. R.; Tsang, S.-W.; Shi, T.; et al. Optimizing Crystallization in Wide-Bandgap Mixed Halide Perovskites for High-Efficiency Solar Cells. *Adv. Mater.* **2024**, *36* (17), 2306568.
(18) He, Q.; Wang, J.; Wu, M.; Zhong, C.; Li, L.; Zhao, X.; Ding, M.; Yang, P.; Li, R.; Huang, W.; et al. A Self-Assembled Molecule Directs Ordered α-FAPbI3 for n-i-p Perovskite Solar Cells. *Nat. Commun.* **2026**, *17*, 1479.
(19) Chen, S.; Xiao, X.; Chen, B.; Kelly, L. L.; Zhao, J.; Lin, Y.; Toney, M. F.; Huang, J. Crystallization in One-Step Solution Deposition of Perovskite Films: Upward or Downward? *Sci. Adv* **2021**, *7* (4), No. eabb2412.
(20) Chen, B.; Rudd, P. N.; Yang, S.; Yuan, Y.; Huang, J. Imperfections and Their Passivation in Halide Perovskite Solar Cells. *Chem. Soc. Rev.* **2019**, *48* (14), 3842−3867.
(21) Wu, J.; Li, M. H.; Fan, J. T.; Li, Z.; Fan, X. H.; Xue, D. J.; Hu, J.-S. Regioselective Multisite Atomic-Chlorine Passivation Enables Efficient and Stable Perovskite Solar Cells. *J. Am. Chem. Soc.* **2023**, *145* (10), 5872−5879.
(22) Li, C.; Zhang, N.; Gao, P. Lessons Learned: How to Report XPS Data Incorrectly about Lead-Halide Perovskites. *Mater. Chem. Front.* **2023**, *7* (18), 3797−3802.
(23) Park, S. M.; Wei, M.; Lempesis, N.; Yu, W.; Hossain, T.; Agosta, L.; Carnevali, V.; Atapattu, H. R.; Serles, P.; Eickemeyer, F. T.; Shin, H.; Vafaie, M.; Choi, D.; Darabi, K.; Jung, E. D.; Yang, Y.; Kim, D. B.; Zakeeruddin, S. M.; Chen, B.; Amassian, A.; Filleter, T.; Kanatzidis, M. G.; Graham, K. R.; Xiao, L.; Rothlisberger, U.; Grätzel, M.; Sargent, E. H. Low-Loss Contacts on Textured Substrates for Inverted Perovskite Solar Cells. *Nature* **2023**, *624*, 289−294.
(24) Wu, S.; Zhang, J.; Li, Z.; Liu, D.; Qin, M.; Cheung, S. H.; Lu, X.; Lei, D.; So, S. K.; Zhu, Z.; Jen, A. K. Y. Modulation of Defects and Interfaces through Alkylammonium Interlayer for Efficient Inverted Perovskite Solar Cells. *Joule* **2020**, *4* (6), 1248−1262.
(25) Shao, Y.; Xiao, Z.; Bi, C.; Yuan, Y.; Huang, J. Origin and Elimination of Photocurrent Hysteresis by Fullerene Passivation in $CH_3NH_3PbI_3$ Planar Heterojunction Solar Cells. *Nat. Commun.* **2014**, *5*, 5784.
(26) Chen, J.; Zhu, G. P.; Wang, K. L.; Chen, C. H.; Teng, T. Y.; Xia, Y.; Wang, T.; Wang, Z. K. Unveiling Full-Dimensional Distribution of Trap States toward Highly Efficient Perovskite Photovoltaics. *eScience* **2025**, *5* (2), 100326.
(27) Chen, J.; Su, Z.-H.; Song, B.; Wang, K.-L.; Lv, Q.; Chen, C.-H.; Xia, Y.; Huang, L.; Wang, Z.-K. Surface Template Realizing Oriented Perovskites for Highly Efficient Solar Cells. *Adv. Mater.* **2025**, *37* (15), 2417054.
(28) Oner, S. M.; Sezen, E.; Yordanli, M. S.; Karakoc, E.; Deger, C.; Yavuz, I. Surface Defect Formation and Passivation in Formamidinium Lead Triiodide ($FAPbI_3$) Perovskite Solar Cell Absorbers. *J. Phys. Chem. Lett.* **2022**, *13* (1), 324−330.
(29) Yin, W.-J.; Shi, T.; Yan, Y. Unusual Defect Physics in $CH_3NH_3PbI_3$ Perovskite Solar Cell Absorber. *Appl. Phys. Lett.* **2014**, *104*, 063903.
(30) Ma, K.; Sun, J.; Atapattu, H. R.; Larson, B. W.; Yang, H.; Sun, D.; Chen, K.; Wang, K.; Lee, Y.; Tang, Y.; et al. Holistic Energy Landscape Management in 2D/3D Heterojunction via Molecular Engineering for Efficient Perovskite Solar Cells. *Sci. Adv.* **2023**, *9* (23), No. eadg0032.
(31) Cao, Q.; Li, Y.; Zhang, H.; Yang, J.; Han, J.; Xu, T.; Wang, S.; Wang, Z.; Gao, B.; Zhao, J.; et al. Efficient and Stable Inverted Perovskite Solar Cells with Very High Fill Factors via Incorporation of Star-Shaped Polymer. *Sci. Adv.* **2021**, *7* (28), No. eabg0633.
(32) Caprioglio, P.; Wolff, C. M.; Sandberg, O. J.; Armin, A.; Rech, B.; Albrecht, S.; Neher, D.; Stolterfoht, M. On the Origin of the Ideality Factor in Perovskite Solar Cells. *Adv. Energy Mater.* **2020**, *10* (27), 2000502.
(33) Li, B.; Deng, J.; Smith, J. A.; Caprioglio, P.; Ji, K.; Luo, D.; McGettrick, J. D.; Jayawardena, K. D. G. I.; Kilbride, R. C.; Ren, A.; et al. Suppressing Interfacial Recombination with a Strong-Interaction Surface Modulator for Efficient Inverted Perovskite Solar Cells. *Adv. Energy Mater.* **2022**, *12* (48), 2202868.
(34) Kirchartz, T.; Rau, U. What Makes a Good Solar Cell? *Adv. Energy Mater.* **2018**, *8* (28), 1703385.
(35) Li, N.; Niu, X.; Chen, Q.; Zhou, H. Towards Commercialization: The Operational Stability of Perovskite Solar Cells. *Chem. Soc. Rev.* **2020**, *49* (22), 8235−8286.
(36) Khenkin, M. V.; Katz, E. A.; Abate, A.; Bardizza, G.; Berry, J. J.; Brabec, C.; Brunetti, F.; Bulović, V.; Burlingame, Q.; Di Carlo, A.; et al. Consensus Statement for Stability Assessment and Reporting for Perovskite Photovoltaics Based on ISOS Procedures. *Nat. Energy* **2020**, *5* (1), 35−49.
(37) Li, B.; Deng, J.; Jayawardena, K. D. G. I.; Liu, X.; Xiang, Y.; Ren, A.; Oluwabi, A. T.; Hinder, S.; Putland, B.; Watts, J. F.; et al. Unraveling the Degradation Pathway of Inverted Perovskite Solar Cells Based on ISOS-D-1 Protocol. *Small Methods* **2023**, *8*, 2300223.

https://doi.org/10.1021/jacs.6c02548
J. Am. Chem. Soc. 2026, 148, 13433−13443